Advances in Nano Research, *Vol. 12, No. 2 (2022) 213-221*
https://doi.org/10.12989/anr.2022.12.2.213

Electronic properties of monolayer silicon carbide nanoribbons using tight-binding approach

M.W. Chuan, Y.B. Wong, A. Hamzah, N.E. Alias, S. Mohamed Sultan, C.S. Lim and M.L.P. Tan*

School of Electrical Engineering, Faculty of Engineering, Universiti Teknologi Malaysia, 81310 Skudai, Johor, Malaysia

(*Received July 26, 2021, Revised December 18, 2021, Accepted December 28, 2021*)

Abstract. Silicon carbide (SiC) is a binary carbon-silicon compound. In its two-dimensional form, monolayer SiC is composed of a monolayer carbon and silicon atoms constructed as a honeycomb lattice. SiC has recently been receiving increasing attention from researchers owing to its intriguing electronic properties. In this present work, SiC nanoribbons (SiCNRs) are modelled and simulated to obtain accurate electronic properties, which can further guide fabrication processes, through bandgap engineering. The primary objective of this work is to obtain the electronic properties of monolayer SiCNRs by applying numerical computation methods using nearest-neighbour tight-binding models. Hamiltonian operator discretization and approximation of plane wave are assumed for the models and simulation by applying the basis function. The computed electronic properties include the band structures and density of states of monolayer SiCNRs of varying width. Furthermore, the properties are compared with those of graphene nanoribbons. The bandgap of ASiCNR as a function of width are also benchmarked with published DFT-GW and DFT-GGA data. Our nearest neighbour tight-binding (NNTB) model predicted data closer to the calculations based on the standard DFT-GGA and underestimated the bandgap values projected from DFT-GW, which takes in account the exchange-correlation energy of many-body effects.
Keywords: bandgap engineering; electronic properties; monolayer; nanoribbon; silicon carbide; tight-binding

1. Introduction

Owing to their extraordinary electronic and mechanical properties, graphene nanoribbons (GNRs) have become the most common and well-known material in the semiconductor industry since 2004 (Novoselov *et al*. 2004). GNRs can be experimentally prepared by patterning epitaxially synthesised graphene (Geim and Novoselov 2007). In the laboratory, mechanically exfoliated graphene can be cut into GNRs. The success of using graphene has led to the studies on other 2D materials such as silicon carbide (SiC) (Zhang *et al*. 2017). Uniformly doped structures (Chuan *et al*. 2020) are among the materials that can induce bandgap in gapless materials.

SiC forms into various crystal structures. Examples include ribbons, linear chains, zincblende crystals, and honeycomb sheets. In monolayer SiC Nanoribbons (SiCNR), the silicon and carbon atoms form a graphene-like honeycomb structure. The silicon and carbon atoms in the monolayer SiC bond through the sp2 hybrid orbitals (Chabi and Kadel 2020). Moreover, recent studies have shown that the planar structure of 2D SiC with a honeycomb structure is energetically stable (Li *et al*. 2011, Ding and Wang 2014, Shi *et al*. 2015, Chabi *et al*. 2016, Fan *et al*. 2017). The planar honeycomb monolayer materials are also known as siligraphene comprises several atomic configuration, namely SiC2, SiC3, SiC5, and SiC7 (Hussain *et al*. 2019). Siligraphene is a promising material for a wide range of application including renewable energy storage, gas sensing, lithium ion batteries (LIBs) and hydrogen storage, due to its light weight and exceptional mechanical and electrical capabilities (Dong *et al*. 2016, Naqvi *et al*. 2018, Hussain *et al*. 2019). Monolayer SiCNR can contribute to the future developments of optoelectronic and electronic devices by overcoming the constraints of GNRs or silicene. It is often utilised in high-power, high-temperature, and high-frequency electronics (Harris 1995, Hefner *et al*. 2006, Shen *et al*. 2011).

The density-functional theory (DFT)-based first-principles technique was used to study SiCNRs. Sun *et al*. (2008) used the Perdew-Wang functional (PW91) by employing the generalized-gradient approximation (GGA) exchange correlation technique to investigate hydrogen-terminated SiCN. They discovered that when the width of the material increased, the direct bandgap oscillated and increased regularly, indicating the semiconducting property of SiCNR. First-principles DFT-GGA calculations (Bekaroglu *et al*. 2010) revealed indirect bandgaps ranging from 1.3 eV to 1.7 eV in bare armchair SiCNRs.

Furthermore, first-principles projector-augmented wave potential within the DFT approach was used to investigate the electronic characteristics of SiCNR (Zhang *et al*. 2010). When the width N_a of armchair SiCNR increased, the bandgaps oscillated with a saw-tooth pattern and quenched to a constant value of 2.359 eV. Lin *et al*. (2013) also found that the thickness and geometric arrangement of SiC nanomaterials significantly impact their characteristics. Moreover, the in-plane strain may be used to adjust the direct bandgap of a monolayer 2D SiC. Nevertheless, most previous studies on SiC were performed by using DFT.

*Corresponding author, Ph.D.,
E-mail: michael@utm.my

Copyright © 2022 Techno-Press, Ltd.
http://www.techno-press.org/?journal=journal=anr&subpage=5 ISSN: 2287-237X (Print), 2287-2388 (Online)

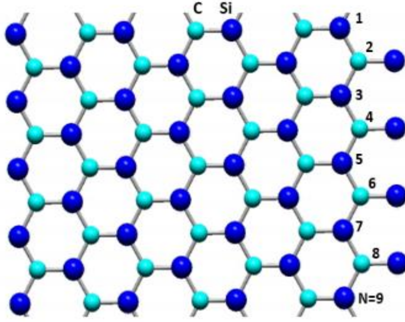

Fig. 1 ASiCNRs structure with N-dimers; the cyan and dark blue spheres represent carbon silicon atoms, respectively

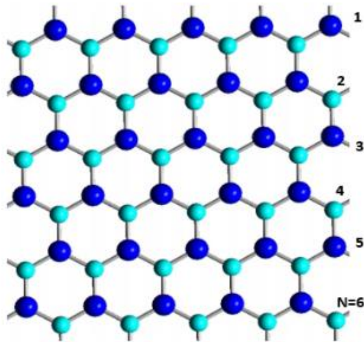

Fig. 2 ZSiCNRs structure with N-dimers; the cyan and dark blue spheres represent carbon silicon atoms, respectively

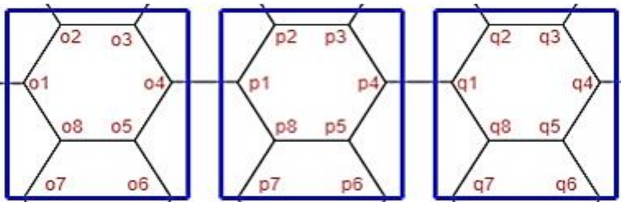

Fig. 3 Schematic diagram of 4-ASiCNRs with length = 3; unit cells are highlighted, and atoms are numbered

In 2010, Zhao *et al*. (2010) studied the electronic structures of SiCNR using tight-binding approach. One of the major discrepancies with present work is that they benchmarked their findings against first-principles calculations whereas we compared our results with DFT. As such, our nearest neighbour tight-binding (NNTB) model uses different on-site energies and hopping integrals parameter that are described in Section 2. Although both tight-binding work explored the effect of widths on the electronics properties, previous work mainly focus on the edge effects by modifying the fitting parameters to fit the highest valence band (HVB) and lowest conduction band (LCB). In present work, we provided comprehensive computational modelling, such as algebraic relationships between Hamiltonian operators in tight binding models where they can be easily replicated for simulations.

Therefore, we developed a model for monolayer SiCNR based on the NNTB and Schrödinger's time-independent equation to investigate the essential electronic properties of SiCNR. We investigated two orientations: the armchair SiCNR (ASiCNR) and zigzag SiCNR (ZSiCNR), as shown in Figs. 1 and 2, respectively.

This remainder of this work consists of three sections. Section 2 presents the mathematical model of the Hamiltonian matrix, band structure, density of states (DOS) of monolayer SiCNR using NNTB. Section 3 details all simulation findings. Finally, Section 4 provides the conclusion based on the findings of the work.

2. Computational model

The theoretical model and methodology, shown in this section, allows researchers to quickly start constructing the Hamiltonian operator matrix by following the concept used in the present work to study the electronic properties of monolayer silicon carbide nanoribbons. Researchers can predict the DOS and band structure upon careful bandgap engineering through NNTB approach with low computational effort. The following subsections present the computational modelling procedures and mathematical equations employed to obtain the band structures and DOS.

2.1 Tight binding model

The NNTB model was used to compute the electronic properties of SiCNRs. The model is based on the Schrödinger equation, shown in Eq. (1), which preserves the wave-like properties of electrons.

$$E\{\Psi\} = [H]\{\Psi\} \tag{1}$$

The physical structure of the model is described by the Hamiltonian operator, H. This operator needs to be defined properly and paired with a suitable wave function, Ψ to obtain the energy spectrum (Oxtoby *et al*. 2015).

2.2 Hamiltonian operator

A Hamiltonian matrix, shown in Eq. (2), can be obtained by defining both the alpha and beta matrices. This approach enables the 2D SiCNR structure to be transformed into a 1D structure.

$$H_{4-ASiCNR\ or\ ZSiCNR\ ,L=3} = \begin{bmatrix} \alpha & \beta & 0 \\ \beta' & \alpha & \beta \\ 0 & \beta' & \alpha \end{bmatrix} \tag{2}$$

This matrix contains α, β, and β' matrices, which represent the self-interacting unit cells, interaction between the unit cells, relationship to the other side of the alpha matrices, respectively. To form the alpha matrix of monolayer ASiCNRs, we used a clockwise sequence in numbering SiC atoms, as shown in Fig. 3.

The off-diagonals of the alpha matrix for the ASiCNRs were filled. However, starting from the 4-ASiCNRs, an additional hopping interaction between the SiC atoms from different unit cells, t was added to the alpha matrix because some of the π-orbitals have three nearest bonds within the defined boundary of the unit cell, as shown in Eq. (3).

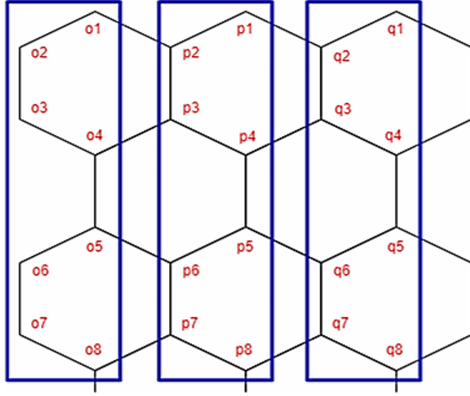

Fig. 4 Schematic diagram of 4-ASiCNRs with length = 3; unit cells are highlighted, and atoms are numbered

Table 1 Computed NNTB model parameters for monolayer SiCNR

Parameters	t	Ec	ESi
Value (eV)	1.637	0	2.627

$$\alpha_{4-ASiCNR} = \begin{array}{c} \\ p1 \\ p2 \\ p3 \\ p4 \\ p5 \\ p6 \\ p7 \\ p8 \end{array} \begin{array}{c} \begin{array}{cccccccc} p1 & p2 & p3 & p4 & p5 & p6 & p7 & p8 \end{array} \\ \begin{bmatrix} \varepsilon_{Si} & t & 0 & 0 & 0 & 0 & 0 & t \\ t & \varepsilon_C & t & 0 & 0 & 0 & 0 & 0 \\ 0 & t & \varepsilon_{Si} & t & 0 & 0 & 0 & 0 \\ 0 & 0 & t & \varepsilon_C & t & 0 & 0 & 0 \\ 0 & 0 & 0 & t & \varepsilon_{Si} & t & 0 & t \\ 0 & 0 & 0 & 0 & t & \varepsilon_C & t & 0 \\ 0 & 0 & 0 & 0 & 0 & t & \varepsilon_{Si} & t \\ t & 0 & 0 & 0 & t & 0 & t & \varepsilon_C \end{bmatrix} \end{array} \qquad (3)$$

For the monolayer ZSiCNRs, the alpha matrix is fairly straightforward. Fig. 4 shows the schematic of 4-ZSiCNR, with blue colour highlighted boxes representing the ZSiCNR unit cells. The boundary unit cell and the labels of the SiC atoms are clearly shown in Fig. 4.

In the 4-ZSiCNRs structure, there are four silicon atoms and four carbon atoms arranged accordingly. Hence, seven π-orbitals are formed within the unit cell. The alpha matrix of the unit cell p for the 4-ZSiCNR is

$$\alpha_{4-ZSiCNR} = \begin{array}{c} \\ p1 \\ p2 \\ p3 \\ p4 \\ p5 \\ p6 \\ p7 \\ p8 \end{array} \begin{array}{c} \begin{array}{cccccccc} p1 & p2 & p3 & p4 & p5 & p6 & p7 & p8 \end{array} \\ \begin{bmatrix} \varepsilon_{Si} & t & 0 & 0 & 0 & 0 & 0 & 0 \\ t & \varepsilon_C & t & 0 & 0 & 0 & 0 & 0 \\ 0 & t & \varepsilon_{Si} & t & 0 & 0 & 0 & 0 \\ 0 & 0 & t & \varepsilon_C & t & 0 & 0 & 0 \\ 0 & 0 & 0 & t & \varepsilon_{Si} & t & 0 & t \\ 0 & 0 & 0 & 0 & t & \varepsilon_C & t & 0 \\ 0 & 0 & 0 & 0 & 0 & t & \varepsilon_{Si} & t \\ 0 & 0 & 0 & 0 & t & 0 & t & \varepsilon_C \end{bmatrix} \end{array} \qquad (4)$$

The interaction between the unit cells is represented by the beta matrix. In particular, the beta matrix considers the interaction sites of the π-orbitals between the unit cells. The beta matrices of 4-ASiCNR and 4-ZSiCNR are given by Eqs. (5) and (6), respectively. For the monolayer ASiCNR, the interaction between unit cell p and unit cell q are shown in the Eq. (5). The beta matrix of ZSiCNR is similar to that of ASiCNR, shown in Eq. (6). In addition, the relationship to the other side of the alpha matrix of ASiCNR can be obtained by transposing the beta matrices.

$$B_{4-ASiCNR} = \begin{array}{c} \\ p1 \\ p2 \\ p3 \\ p4 \\ p5 \\ p6 \\ p7 \\ p8 \end{array} \begin{array}{c} \begin{array}{cccccccc} q1 & q2 & q3 & q4 & q5 & q6 & q7 & q8 \end{array} \\ \begin{bmatrix} 0 & 0 & 0 & 0 & 0 & 0 & 0 & 0 \\ 0 & 0 & 0 & 0 & 0 & 0 & 0 & 0 \\ 0 & 0 & 0 & 0 & 0 & 0 & 0 & 0 \\ t & 0 & 0 & 0 & 0 & 0 & 0 & 0 \\ 0 & 0 & 0 & 0 & 0 & 0 & 0 & 0 \\ 0 & 0 & 0 & 0 & 0 & 0 & t & 0 \\ 0 & 0 & 0 & 0 & 0 & 0 & 0 & 0 \\ 0 & 0 & 0 & 0 & 0 & 0 & 0 & 0 \end{bmatrix} \end{array} \qquad (5)$$

$$B_{4-ZSiCNR} = \begin{array}{c} \\ p1 \\ p2 \\ p3 \\ p4 \\ p5 \\ p6 \\ p7 \\ p8 \end{array} \begin{array}{c} \begin{array}{cccccccc} q1 & q2 & q3 & q4 & q5 & q6 & q7 & q8 \end{array} \\ \begin{bmatrix} 0 & t & 0 & 0 & 0 & 0 & 0 & 0 \\ 0 & 0 & 0 & 0 & 0 & 0 & 0 & 0 \\ 0 & 0 & 0 & 0 & 0 & 0 & 0 & 0 \\ 0 & 0 & t & 0 & 0 & 0 & 0 & 0 \\ 0 & 0 & 0 & 0 & 0 & t & 0 & 0 \\ 0 & 0 & 0 & 0 & 0 & 0 & 0 & 0 \\ 0 & 0 & 0 & 0 & 0 & 0 & 0 & 0 \\ 0 & 0 & 0 & 0 & 0 & 0 & t & 0 \end{bmatrix} \end{array} \qquad (6)$$

The hopping integral between neighbouring π-orbitals of SiC atoms or between unit cells, t is 1.637 eV, whereas the on-site energies for carbon and silicon are $E_c = 0\ eV$ and $E_{Si} = 2.627\ eV$ (Qin *et al*. 2015), respectively, as shown in Table 1.

2.3 Density of states

Localised DOS, $LDOS(E)$, is the number of states occupied at a certain energy interval in a unit cell. The localised DOS can be simulated numerically by using the delta function, δ (Datta 2005). The localised DOS is computed by using Eq. (7).

$$LDOS(E) = \sum_{i=1}^{N} \frac{1}{2\pi} \int \delta[E_i(k) - E]dk \qquad (7)$$

where the delta function, δ is given by Eq. (8). Substitution of Eq. (8) into Eq. (7) leads to Eq. (9).

$$\delta[E_i(k) - E] = \frac{\eta_G}{[E_i(k) - E]^2 + {\eta_G}^2} \qquad (8)$$

$$Local\ DOS(E) = \sum_{i=1}^{N} \frac{1}{2\pi} \sum_{all\ k} \frac{\eta_G}{[E_i(k) - E]^2 + {\eta_G}^2} \qquad (9)$$

Green's function DOS can be calculated by using the Green's function theory (Datta 1997) given by Eq. (10), where G_F indicates the retarded Green's function, Eq. (11). The η in Eq. (11), represents a small imaginary value. The existence of η prevents the divergence of the inverse matrix. The identify matrix and Hamiltonian operator

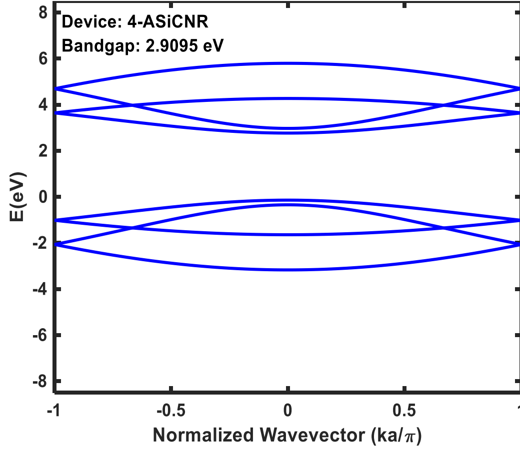

Fig. 5 Band structure of 4-ASiCNR

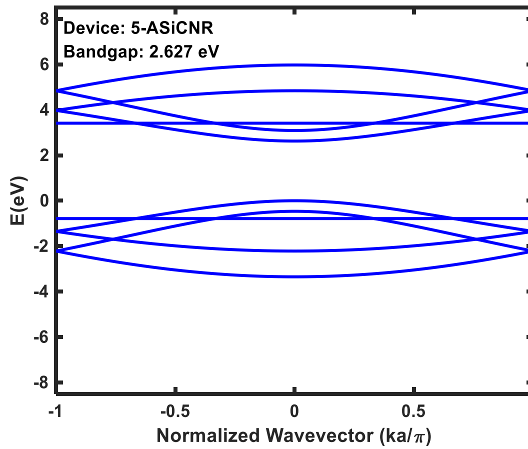

Fig. 6 Band Structure of 5-ASiCNR

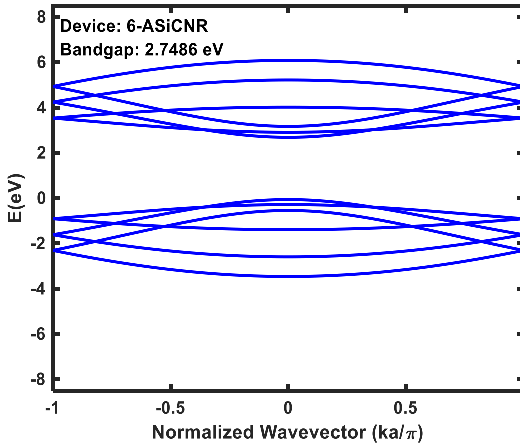

Fig. 7 Band Structure of 6-ASiCNR

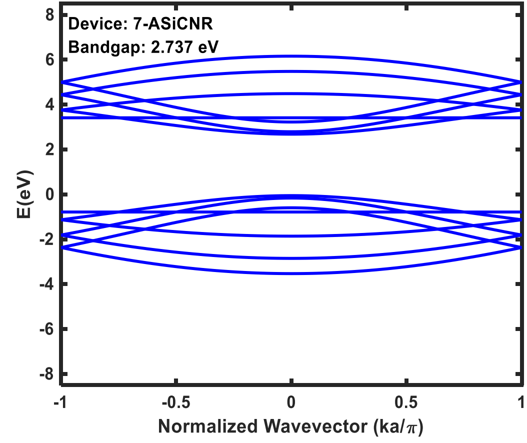

Fig. 8 Band Structure of 7-ASiCNR

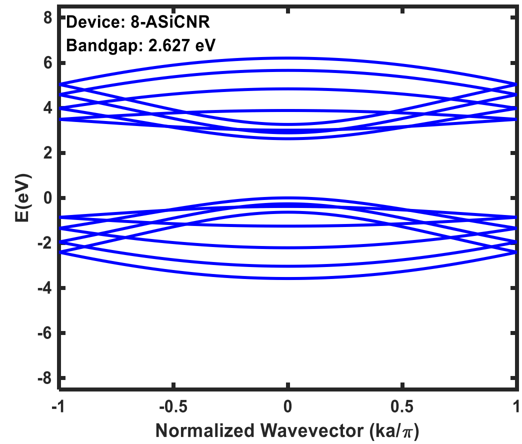

Fig. 9 Band Structure of 8-ASiCNR

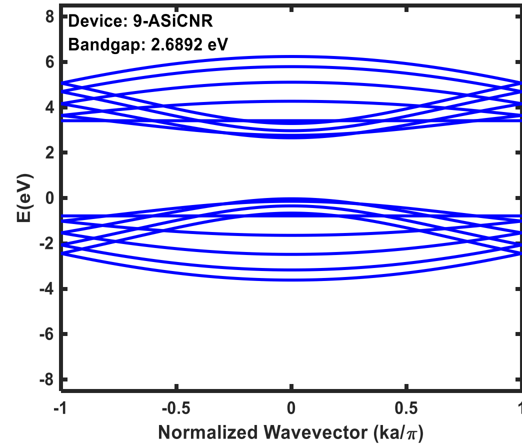

Fig. 10 Band Structure of 9-ASiCNR

matrices are represented by I and H (Wong *et al.* 2019), respectively.

$$E\{\Psi\} = [H]\{\Psi\}\ Green's\ Function\ DOS = \frac{1}{\pi} Im(Trace[G_F]) \quad (10)$$

$$G^{retarted} = [(E + i\eta) * I - H]^{-1} \quad (11)$$

3. Results and discussion

This section is divided into three parts. The band structures and DOS of SiCNRs are shown first, followed by a discussion of the results relative to the GNRs.

3.1 Band structure of monolayer SiCNR

The computational procedures described in Section 2 were used to simulate the band structures of monolayer

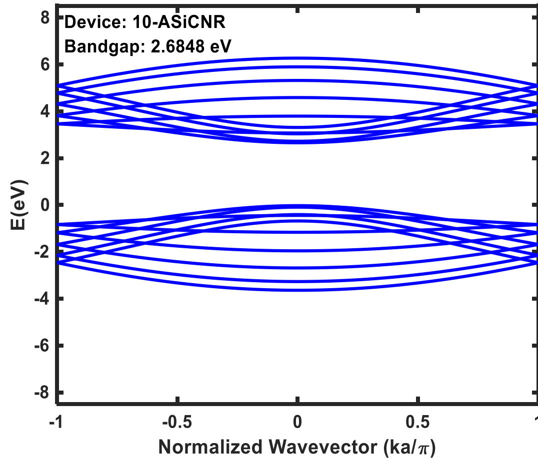

Fig. 11 Band Structure of 10-ASiCNR

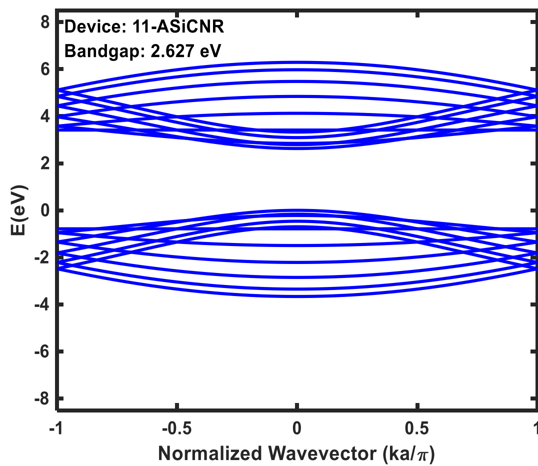

Fig. 12 Band Structure of 11-ASiCNR

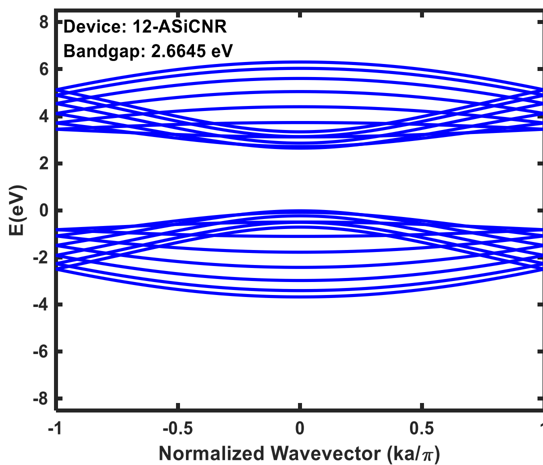

Fig. 13 Band Structure of 12-ASiCNR

Table 2 Benchmark of bandgap against published work for the three distinct groups of ASiCNRs

N_a	$E_{NNTB}(eV)$	$E_{GGA}(eV)$	$E_{GW}(eV)$
6(3p)	2.75	2.41	4.18
7(3p + 1)	2.74	2.38	4.17
8(3p + 2)	2.63	2.31	3.90

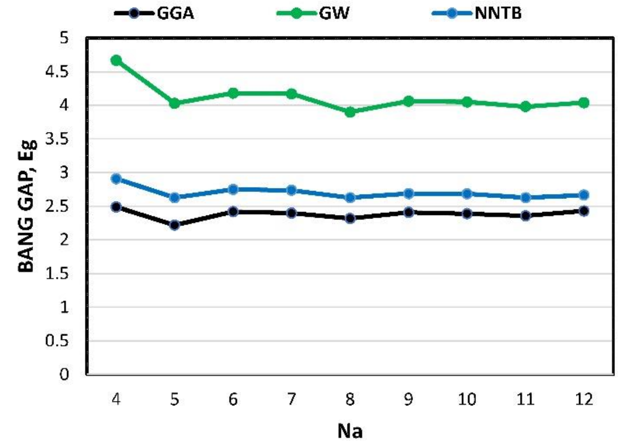

Fig. 14 Bandgap of ASiCNR as a function of width N_a. Green, black, and blue lines represent the GW, GGA, and NNTB results, respectively. The GW and GGA results were obtained from (Alaal *et al*. 2016), whereas the NNTB results are from this present work.

ASiCNR with varying widths, N_a. In a previous study (Shukla *et al*. 2016), DFT-GGA and DFT-GW approximations were used to investigate ASiCNR with three distinct width families, namely $N_a = 3p, 3p + 1, 3p + 2$ (p is a positive integer), with N_a values varied between 4 and 12. We benchmarked our findings against these published results (Shukla *et al*. 2016). In Figs. 5-13, we present the band structures for 4-ASiCNR, 5-ASiCNR, 6-ASiCNR, 7-ASiCNR, 8-ASiCNR, 9-ASiCNR, 10-ASiCNR, 11-ASiCNR, and 12-ASiCNR, respectively. The names of the structures follow this notation: N_a-ASiCNR.

When the ribbon width, N_a, increased from 4 to 12, the bandgap value decreased gradually from 2.9095 eV to 2.6645 eV. This reduction is due to the quantum confinement effect across the ribbon width. According to Table 2, the family behaviour of NNTB bandgaps follow this hierarchy: $E_g(3_p) > E_g(3_p + 1) > E_g(3_p + 2)$, which is consistent with previous DFT-GGA and DFT-GW approximation studies (Alaal, Loganathan *et al*. 2016).

In Fig. 14, the oscillatory behaviour of bandgaps with N_a appears similar for all the methods. However, the values derived from the present work is different from the DFT results. This difference indicates that the NNTB is less precise than DFT-GW but much closer to DFT-GGA approximation studies. This inaccuracy is mainly because several assumptions were made for the NNTB model to simplify the calculation procedures namely the exclusion of exchange and correlation energy which are accounted for DFT calculations. The other assumptions are the basis function which describes the wavefunction of electrons in the molecules that will transport themselves and are unrelated to the rest of the valence band electrons. These wavefunctions are only affected by the adjacent neighbours (Goh *et al*. 2018). The energy spectrum is also assumed to be discretized into a matrix equation. In addition, we assumed that the chemical surroundings of the atoms on both edges are always similar to that of atoms in the

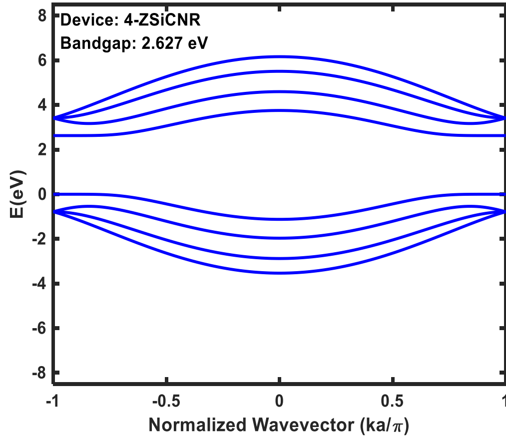

Fig. 15 Band structure of 4-ZSiCNR, L = 3

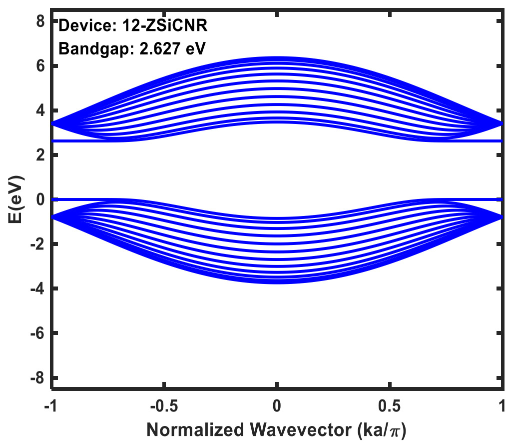

Fig. 16 Band structure of 12-ZSiCNR, L = 3

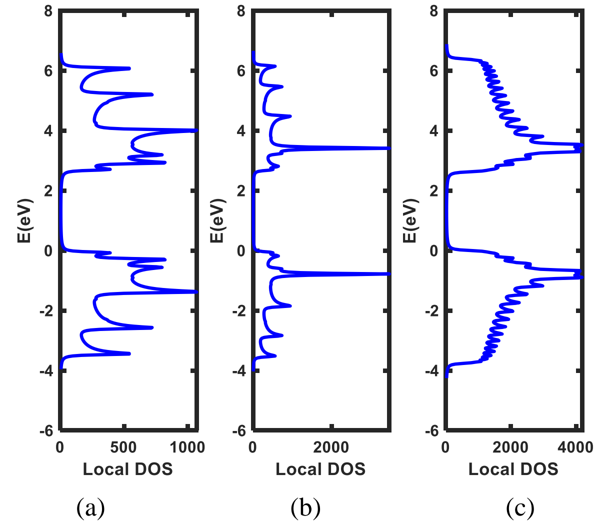

Fig. 17 DOS plot: (a) 6-ASiCNR, (b) 7-ASiCNR, and (c) 30-ASiCNR

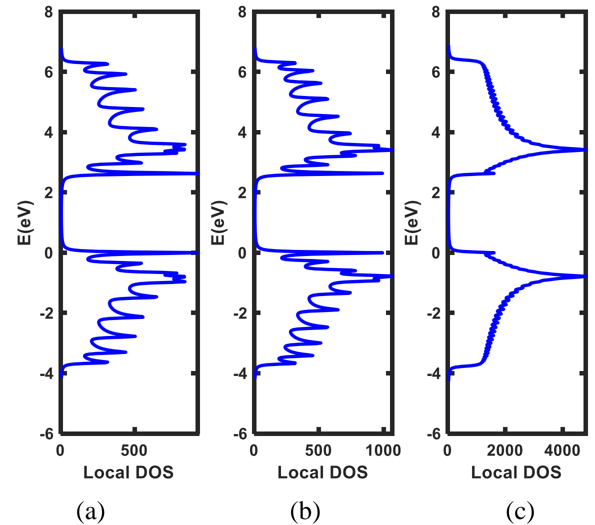

Fig. 18 DOS plot: (a) 6-ZSiCNR, (b) 7-ZSiCNR, and (c) 30-ZSiCNR

centre. As a result, the on-site energies of the edge atoms and hopping integrals are always the same as those of the centre atoms.

The band structures of monolayer ZSiCNR with varying widths were also simulated. The shape of the band structures and the bandgaps of ZSiCNRs remain the same for all widths, owing to the degeneracy of the sub-band structure at k = 0.7. Figs. 15 and 16 show the band structures of 4-ZSiCNR and 12-ZSiCNR, respectively. The observed discrepancy from these figures is the increasing number of bands as the width of ZSiCNR increases. It is revealed that the bandgap predicted by DFT-GW approximation is much higher because it captures the many-body effects in a quantum system. When a standard DFT-GGA is employed, minimal differences with NNTB in bandgap calculation are recorded.

3.2 Density of states

The numerical DOS was simulated for specific widths. However, numerical DOS method is length-independent and varies only with the widths. Figs. 17 and 18 show the numerical DOS of monolayer ASiCNR and ZSiCNR, respectively, with different widths equal to 6, 7, and 30. The number of peaks in the DOS plot increases when the width increases.

By comparing the band structure with the DOS of 5-ASiCNR in Fig. 19, we observed that the highest peak in the DOS is caused by the crossing of several sub-bands in the band structure at approximately 3.41 eV. The intense peak at this specific energy level indicates that many states are available for occupation by electrons. When the width increases to 20 (Fig. 20), the size of the nanoribbon and the number of atoms and sub-bands also increase. More sub-bands cross each other, leading to more visible, prominent peaks in the DOS. Consequently, the overall DOS also increases with SiCNR widths.

Green's function theory can be used to compute the DOS of monolayer SiCNR. The DOS obtained by this method is length-dependent. Figs. 21 and 22 show the Green's function DOS of monolayer ASiCNR and ZSiCNR, respectively, with different lengths equal to 1, 10, and 50. Based on our simulation results, the DOS differed significantly when the length increased from 1 to 10. However, when the nanoribbon length is sufficiently long (L = 50), the DOS started to converge to a similar form.

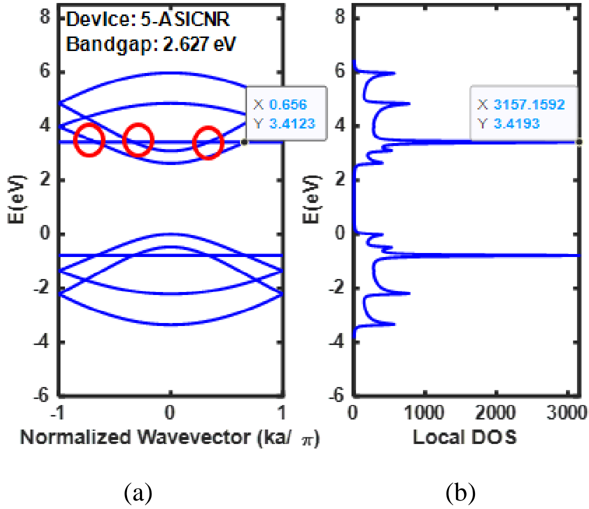

(a) (b)

Fig. 19 (a) Band structure and (b) DOS of 5-ASiCNR

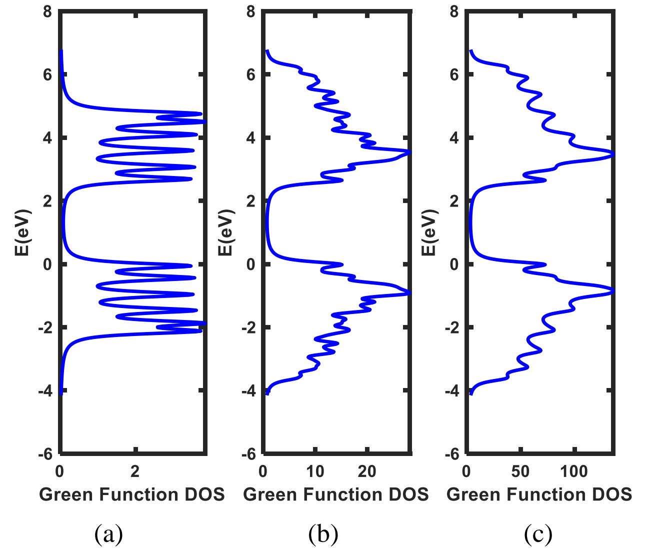

(a) (b) (c)

Fig. 22 Green's function DOS for 6-ZSiCNR: (a) L=1, (b) L = 10, and (c) L = 50

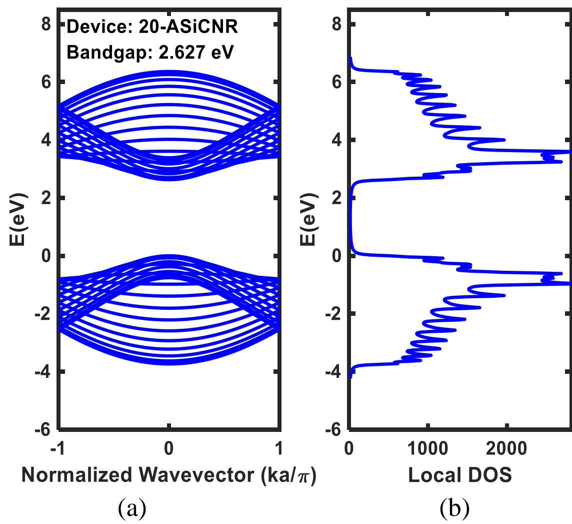

(a) (b)

Fig. 20 (a) Band structures and (b) DOS plot of 20-ASiCNR

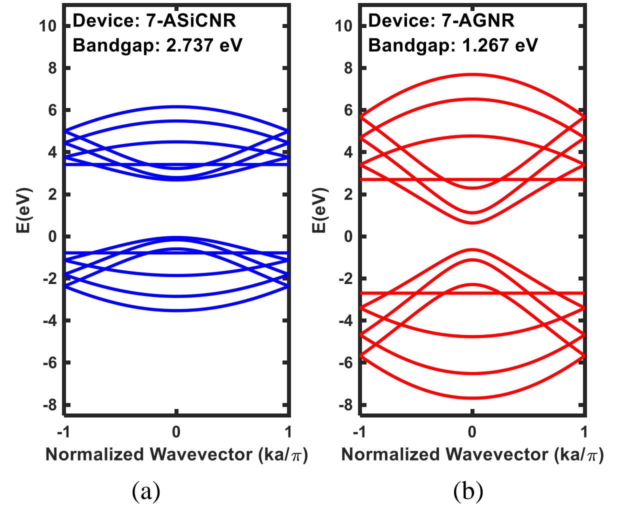

(a) (b)

Fig. 23 Band structures for (a) 7-ASiCNR and (b) 7-AGNR

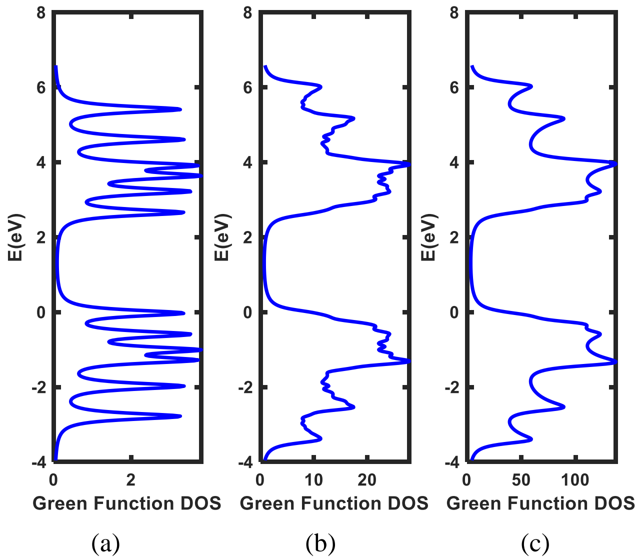

(a) (b) (c)

Fig. 21 Green's function DOS for 6-ASiCNR: (a) L = 1, (b) L = 10, and (c) L = 50

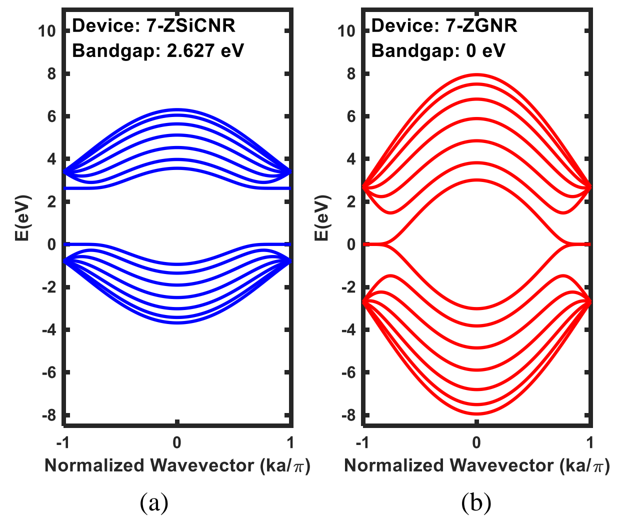

(a) (b)

Fig. 24 Band structures for (a) 7-ZSiCNR and (b) 7-ZGNR

Table 3 Comparison of bandgap for three distinct groups between ASiCNR and AGNR

N_a	E_g for ASiCNR (eV)	E_g for AGNR (eV)
$6(3p)$	2.7486	1.227
$7(3p+1)$	2.737	1.267
$8(3p+2)$	2.627	0

3.3 Comparing monolayer SiCNR with GNR

We compared the monolayer SiCNR and GNR in terms of their electronic properties through their band structures. Our simulation results are shown in Figs. 23 (for armchair-edge orientation) and 24 (for zigzag-edge orientation), where the red and blue lines indicate the band structures of 7-GNR and monolayer 7-SiCNR, respectively.

As shown in Fig. 23, 7-ASiCNR has a larger bandgap at 2.737 eV compared to 7-AGNR at 1.267 eV. For zigzag-edge orientation in Fig. 24, SiCNR is a semiconductor with 2.627 eV bandgap, whereas GNR is metallic due to missing bandgap. It is also demonstrated that the bandgap for three distinct groups in ASiCNR remain quite steadily similar unlike for AGNR where the bandgap abruptly changes. It is noticeable that at the same width, SiCNRs depict smaller bandgap than GNRs for both armchair and zigzag-edged orientations at the conduction and valence band. Goh *et al.* (2018) found that GNRs exhibited three family behaviours for AGNRs.

Table 3 compares the bandgaps between monolayer ASiCNR and GNR for three family groups of width. The bandgap of monolayer ASiCNR follows $E_g(3_\mathrm{p}) > E_g(3_\mathrm{p}+1) > E_g(3_\mathrm{p}+2)$, whereas that of GNR follows $E_g(3_\mathrm{p}+1) > E_g(3_\mathrm{p}) > E_g(3_\mathrm{p}+2)$.

The comparison shows that SiCNR is quite similar to GNR, albeit with a wider bandgap. This observation indicates that SiCNR can function at significantly higher voltages, frequencies, and temperatures than other traditional semiconductors (Harris 1995). It is preferable to use SiCNRs in high-power applications (Xu *et al.* 2019) and optoelectronic devices (Zhang *et al.* 2017). Interestingly, the bandgap of the monolayer SiCNRs can be easily tailored by varying their widths. Moreover, the inter-subbands transitions in SiCNRs between the subsequent subbands yield smaller transition energy due to it narrower gaps in the subbands, compared with those of GNRs. These unique properties of SiCNRs would enable bandgap engineering of SiCNRs to fit specific optoelectronic applications, such as light-emitting diodes, lasers, optoelectronic switches, and solar cells. Furthermore, the electronic properties obtained in this work may be applied for higher design abstraction levels, such as in device and circuit (Chuan *et al.* 2021a, b) levels.

4. Conclusions

The electronic properties of monolayer SiCNR with armchair and zigzag-edged orientations were successfully obtained by using the numerical NNTB model. These properties include band structures, bandgaps, and DOS. For ASiCNR, we can conclude that the overall bandgaps decrease as ribbon widths increase owing to the confinement effect across the ribbon width. For ZSiCNR, we observed a direct bandgap that remained constant for all ribbon widths. Localised numerical DOS vary with the width regardless of length, whereas Green's function DOS are width- and length-dependent. Both DOS converge to a similar shape when the width or length is sufficiently large. Moreover, the present work is benchmarked against published DFT results. It is found that minimal bandgap differences are achieved when NNTB is benchmarked with DFT-GGA approach, although NNTB is found to be less precise than DFT-GW. Nevertheless, NNTB is a more comprehensive modelling approach and it requires less computational cost, compared to DFT studies. In addition, monolayer SiCNRs are more suitable for high-power, high-temperature, and high-frequency electronics owing to its wider bandgap compared to their GNRs counterparts.

Acknowledgement

This work was supported and funded by the Ministry of Higher Education under the Fundamental Research Grant Scheme (FRGS/1/2021/STG07/UTM/02/3). The authors acknowledge the Research Management Centre (RMC), School of Graduate Studies (SPS), and School of Electrical Engineering (SKE) of Universiti Teknologi Malaysia (UTM) for providing excellent support and stimulating research environment.

References

Alaal, N., Loganathan, V., Medhekar, N. and Shukla, A. (2016), "First principles many-body calculations of electronic structure and optical properties of SiC nanoribbons", *J. Phys.*, **49**(10), 105306. https://doi.org/10.1088/0022-3727/49/10/105306.

Bekaroglu, E., Topsakal, M., Cahangirov, S. and Ciraci, S. (2010), "First-principles study of defects and adatoms in silicon carbide honeycomb structures", *Phys. Rev. B.*, **81**(7), 075433. https://doi.org/10.1103/PhysRevB.81.075433.

Chabi, S., Chang, H., Xia, Y. and Zhu, Y. (2016), "From graphene to silicon carbide: Ultrathin silicon carbide flakes", *Nanotechnology*, **27**(7), 075602. https://doi.org/10.1088/0957-4484/27/7/075602.

Chabi, S. and Kadel, K. (2020), "Two-dimensional silicon carbide: Emerging direct band gap semiconductor", *Nanomaterials*, **10**(11), 2226. https://doi.org/10.3390/nano10112226.

Chuan, M., Wong, K., Hamzah, A., Rusli, S., Alias, N., Lim, C. and Tan, M. (2020), "Two-dimensional modelling of uniformly doped silicene with aluminium and its electronic properties", *Adv. Nano Res.*, **9**(2), 105-112. https://doi.org/10.12989/anr.2020.9.2.105.

Chuan, M.W., Wong, K.L., Hamzah, A., Rusli, S., Alias, N.E., Lim, C.S. and Tan, M.L.P. (2021a), "Device modelling and performance analysis of two-dimensional AlSi3 ballistic nanotransistor", *Adv. Nano Res.*, **10**(1), 91-99. https://doi.org/10.12989/anr.2021.10.1.091.

Chuan, M.W., Wong, K.L., Riyadi, M.A., Hamzah, A., Rusli, S., Alias, N.E., Lim, C.S. and Tan, M.L.P. (2021b), "Semi-analytical modelling and evaluation of uniformly doped silicene nanotransistors for digital logic gates", *PloS One*, **16**(6), e0253289. https://doi.org/10.1371/journal.pone.0253289.

Datta, S. (1997), *Electronic Transport in Mesoscopic Systems*, Cambridge University Press, Cambridge, U.K. https://doi.org/10.1017/CBO9780511805776.

Datta, S. (2005), *Quantum transport: Atom to Transistor*, Cambridge University Press, Cambridge, U.K. https://doi.org/10.1017/CBO9781139164313.

Ding, Y. and Wang, Y. (2014), "Geometric and Electronic Structures of Two-Dimensional SiC3 Compound", *J. Phys. Chem. C*, **118**(8), 4509-4515. https://doi.org/10.1021/jp412633y.

Dong, H., Zhou, L., Frauenheim, T., Hou, T., Lee, S.T. and Li, Y. (2016), "SiC7 siligraphene: A novel donor material with extraordinary sunlight absorption", *Nanoscale*, **8**(13), 6994-6999. https://doi.org/10.1039/C6NR00046K.

Fan, D., Lu, S., Guo, Y. and Hu, X. (2017), "Novel bonding patterns and optoelectronic properties of the two-dimensional SixCy monolayers", *J. Mater. Chem. C*, **5**(14), 3561-3567. https://doi.org/10.1039/C6TC05415C.

Geim, A.K. and Novoselov, K.S. (2007), "The rise of graphene", *Nat. Mater.*, **6**(3), 183-191. https://doi.org/10.1038/nmat1849.

Goh, E., Chin, H.C., Wong, K.L., Indra, I.S.B. and Tan, M.L.P. (2018), "Modeling and simulation of the electronic properties in graphene nanoribbons of varying widths and lengths using tight-binding hamiltonian", *J. Nanoelectr. Optoelectr.*, **13**(2), 289-300. https://doi.org/10.1166/jno.2018.2206.

Harris, G.L. (1995), *Properties of Silicon Carbide*, INSPEC, IET, London, U.K. https://doi.org/10.5772/615.

Hefner, A., Ryu, S., Hull, B., Berning, D., Hood, C., Ortiz-rodriguez, J.M., Rivera-Lopez, A., Duong, T., Akuffo, A. and Hernandez-Mora, M. (2006). "Recent advances in high-voltage, high-frequency silicon-carbide power devices", *Procededing of the Conference Record of the 2006 IEEE Industry Applications Conference Forty-First IAS Annual Meeting*, Florida, U.S.A., October. https://doi.org/10.1109/IAS.2006.256542.

Hussain, T., Farokh Niaei, A.H., Searles, D.J. and Hankel, M. (2019), "Three-dimensional silicon carbide from siligraphene as a high capacity lithium ion battery anode material", *J. Phys. Chem C*, **123**(45), 27295-27304. https://doi.org/10.1021/acs.jpcc.9b06151.

Li, Y., Li, F., Zhou, Z. and Chen, Z. (2011), "SiC_2 Silagraphene and its one-dimensional derivatives: Where planar tetra-coordinate silicon happens", *J. Am. Chem. Soc.*, **133**(4), 900-908. https://doi.org/10.1021/ja107711m.

Lin, X., Lin, S., Xu, Y., Hakro, A.A., Hasan, T., Zhang, B., Yu, B., Luo, J., Li, E. and Chen, H. (2013), "Ab initio study of electronic and optical behavior of two-dimensional silicon carbide", *J. Mater. Chem C*, **1**(11), 2131-2135. https://doi.org/10.1039/C3TC00629H.

Naqvi, S.R., Hussain, T., Luo, W. and Ahuja, R. (2018), "Metallized siligraphene nanosheets (SiC7) as high capacity hydrogen storage materials", *Nano Res.* **11**(7), 3802-3813. https://doi.org/10.1007/s12274-017-1954-z.

Novoselov, K.S., Geim, A.K., Morozov, S.V., Jiang, D., Zhang, Y., Dubonos, S.V., Grigorieva, I.V. and Firsov, A.A. (2004), "Electric field effect in atomically thin carbon films", *Science*, **306**(5696), 666-669. https://doi.org/10.1126/science.1102896.

Oxtoby, D.W., Gillis, H.P. and Butler, L.J. (2015), *Principles of modern chemistry*, Cengage Learning, Miami, U.S.A.

Qin, X., Liu, Y., Li, X., Xu, J., Chi, B., Zhai, D. and Zhao, X. (2015), "Origin of Dirac cones in SiC silagraphene: A combined density functional and tight-binding study", *J. Phys. Chem. Lett.*, **6**(8), 1333-1339. https://doi.org/10.1021/acs.jpclett.5b00365.

Shen, M., Krishnamurthy, S. and Mudholkar, M. (2011), "Design and performance of a high frequency silicon carbide inverter", *Proceedings of the 2011 IEEE Energy Conversion Congress and Exposition*, Arizona, U.S.A., September. https://doi.org/10.1109/ECCE.2011.6064038.

Shi, Z., Zhang, Z., Kutana, A. and Yakobson, B.I. (2015), "Predicting two-dimensional silicon carbide monolayers", *ACS Nano*, **9**(10), 9802-9809. https://doi.org/10.1021/acsnano.5b02753.

Sun, L., Li, Y., Li, Z., Li, Q., Zhou, Z., Chen, Z., Yang, J. and Hou, J. (2008), "Electronic structures of SiC nanoribbons", *J. Chem. Phys.*, **129**(17), 174114. https://doi.org/10.1063/1.3006431.

Wong, K.L., Chuan, M.W., Alias, N.E., Hamzah, A., Lim, C.S. and Tan, M.L.P. (2019), "Modeling of low-dimensional pristine and vacancy incorporated graphene nanoribbons using tight binding model and their electronic structures", *Adv. Nano Res.*, **7**(3), 209-221. http://doi.org/10.12989/anr.2019.7.3.209.

Xu, J., Gu, L., Ye, Z., Kargarrazi, S. and Rivas-Davila, J.M. (2019), "Cascode GaN/SiC: A wide-bandgap heterogenous power device for high-frequency applications", *IEEE T. Power Electr.*, **35**(6), 6340-6349. https://doi.org/10.1109/TPEL.2019.2954322.

Zhang, J.M., Zheng, F.L., Zhang, Y. and Ji, V. (2010), "First-principles study on electronic properties of SiC nanoribbon", *J. Mater. Sci.*, **45**(12), 3259-3265. https://doi.org/10.1007/s10853-010-4335-5.

Zhang, W.H., Zhang, F.C., Zhang, W.B., Zhang, S.L. and Yang, W. (2017), "First-principle study of the structural, electronic, and optical properties of SiC nanowires", *Chinese Phys. B.*, **26**(5), 057103. https://doi.org/10.1007/s10853-010-4335-5.

Zhao, K., Zhao, M., Wang, Z. and Fan, Y. (2010), "Tight-binding model for the electronic structures of SiC and BN nanoribbons", *Physica E*, **43**(1), 440-445. https://doi.org/10.1016/j.physe.2010.08.025.

CC